Seamless Integration of an Elastomer with Electrode Matrix and its In-Situ Conversion into a Solid State Electrolyte for Robust Li-Ion Batteries

*Matthew M. Ombaba, Ruxandra Vidu, Logeeswaran Veerayah Jayaraman, Mark Triplett, Jonathan Hsu, and M. Saif Islam**

A unique way of robustly integrating an elastomer film onto a graphitic anode and then post-process it into a solid-state electrolyte for lithium-ion battery applications is reported. The mutual solvability of the elastomer and the binder of the graphitic anode (carboxymethyl cellulose, (CMC)) in dimethylformamide facilitates the fusion of the two heterogeneous layers. Dimensional dynamics evolved during the integrated elastomer conversion into a solid electrolyte by liquid electrolyte uptake reveal a notable preferential uniaxial elongation along the normal plane. In contrast, the non-integrated counterpart elongates along the transversal axis. This elastomer exhibits high ionic conductance (≈10–2 S cm^{-1}). Half-cells constructed with our electrolyte integrated electrode exhibit magnificent reduction and oxidation (REDOX) behavior. The efficient charge transfer across the snugly confined semi-solid electrolyte/electrode interface layer leads to a high rate capability of 0.31 mAh cm^{-2} (41 mAh g^{-1}) at 2 C which is double that of a graphitic conventional half-cell. Unlike regular graphitic electrodes which degrade over time, this electrode remains robust, thanks to its propensity to retain its inherent elasticity. This work demonstrates a facile and scalable paradigm, in fabrication of flexible electrolytes that can easily be integrated to 3D devices and opens opportunities for developing structurally conformable batteries of varied geometries.

1. Introduction

In portable electronic devices, the most critical component is arguably the energy storage device.[1] Better and safer high energy storage devices such as lithium-ion (Li-ion) batteries are becoming increasingly crucial as a result of the meteoric rise of humanity's dependability on portable gadgets. Consequently, the search for solid and gel polymeric electrolytes, touted to be safer for Li-ion batteries, is in high gear.[2] An even bigger incentive for Li-ion batteries that incorporate semi-solid and gel electrolytes lies in the automobile industry, whose huge energy demands would potentially require heavy and bulky energy storage devices.[3] In light of these volumetric and gravimetric constraints, future Li-ion batteries would need to be incorporated into the structural components of automobiles.[4] This requisite is highly challenging, as the utilization of flexible and conformable batteries with high structural integrity will be imperative.[5] Although liquid electrolytes would serve this purpose, gravitational implications impede their practicality. Ingenious protocols will need to be developed to avoid pitfalls associated with the manufacturing, packing, and failure of current Li-ion batteries that employ polymeric electrolytes.

Efforts towards developing flexible and improved solid/gel electrolytes have involved the utilization of macroporous elastomeric thermosets infused with liquid electrolytes.[6] A different approach targets block copolymers such as polyurethanes containing soft and hard phases wherein the former phase sustains ion solvability,[7] while the latter provides a structural framework that reinforces its mechanical strength.[8] After liquid electrolyte uptake, the solid electrolytes are sandwiched between two opposite electrodes in place of a cell separator.[9] It has been observed that the stability of the electrode and solid or gel interface in such architecture is low.[10] Further, the uptake of the liquid electrolyte by these elastomers cannot circumvent the tremendous weight and dimensional increments, especially in the transversal plane. These undermine their structural integrity as they turn into fragile gels that are difficult to handle, hence linear unmodified polyurethanes are seldomly used alone.[11] Additionally, high electrolytic salt loading increases the inter-ionic electrostatic forces and its (salt) coordination with the polymer matrix while a decrease in hydrogen bonding between the hard phases

Dr. M. M. Omababa, Dr. L. V. Jayaraman, M. Triplett, J. Hsu, Prof. M. S. Islam
Northern California Nanotechnology Center and Electrical and Computer Engineering
University of California
One shields Avenue, Davis, CA, 95616
E-mail: sislam@ucdavis.edu
Prof. R. Vidu
Department of Chemical Engineering and Material Science
University of California
Davis, One Shields Avenue, Davis, CA, 95616

DOI: 10.1002/adfm.201301124

© 2013 WILEY-VCH Verlag GmbH & Co. KGaA, Weinheim

of the polyurethane occurs, leading to gradual loss of its tensile strength.[12] Cell assembly henceforth becomes a precarious task and imposes scalability impediments.

Conversely, it is generally accepted that the ionic conductivity of polymer and gel electrolytes is largely dependent on their liquid electrolyte uptake.[13] Highly conductive gel/solid electrolytes are obtained by absorbing large amounts of liquid electrolytes rather than mere modification of the host matrix.[14] Thermodynamically, such a state is achieved when the chemical potentials of the liquid inside and outside the host matrix are equal.[15] It therefore follows that researchers have blended such polyurethanes with non-elastomeric polymers[16] and inorganic matrixes and nanoparticles[17] to foster their structural integrity upon high electrolyte uptake and improve ionic conductivity. Min and Wang have however noted that for this to be effective, the two matrices need to be chemically similar as the interfacial adhesion between different phases impedes ion transfer.[18] Further, the use of microporous and nanofiber polyurethane host matrices that can be loaded with more liquid electrolyte has been explored.[19] This protocol imposes a number of tedious material processing steps. It is therefore imperative to strike a balance between improving the structural integrity and increasing the ionic conductance of the solid/gel electrolytes. Ideal polyurethane host matrix or device architecture thereof would seek to maximize liquid uptake without compromising the device stature.

To circumvent these structural and ionic conductance challenges and permit the use of neat polyurethanes, we propose and demonstrate an ingenious means of controlling their perpetual lateral elongation during electrolyte uptake. Theoretically, elastomer stress such as that emanating from electrolyte uptake, induces a free energy adjustment which manifests itself as a volumetric change in order to attain a new equilibrium.[20] This macroscopic mechanism is identical to the changes experienced by a single polymeric chain under a similar perturbation.[21] The Flory Rheiner theory dictates that the chains assume a configuration that maximizes the entropy of the system.[22] In a free standing elastomer film, the chains will preferentially orient themselves along the lateral axis after electrolyte uptake, as illustrated in **Scheme 1**. However, chains in a biaxially constrained system, as demonstrated in this work, preferentially orient themselves along the direction normal to the constraining plane, in order to attain maximum entropy. Incidentally, the latter orientation potentially offers an additional unprecedented benefit by providing an obstacle free ionic conduit, since the inter-chain space is filled with liquid. By contrast, in the former case, the ions have to conduct through the solid polyether rich domains. Further, a biaxial constraint can only be achieved by integrating a host matrix (elastomer film) of negligible thickness, compared to its diameter, with a rigid electrode surface. Further, in order to orient the polymer chains along the normal plane, conversion of the ensemble into an ionically conductive electrolyte by liquid electrolyte uptake must be performed in situ. To the best of our knowledge, this has not been demonstrated. Here, the electrode matrix would provide a structural support to the frail solid/gel electrolyte for easy handling. Further, such a design could permit high

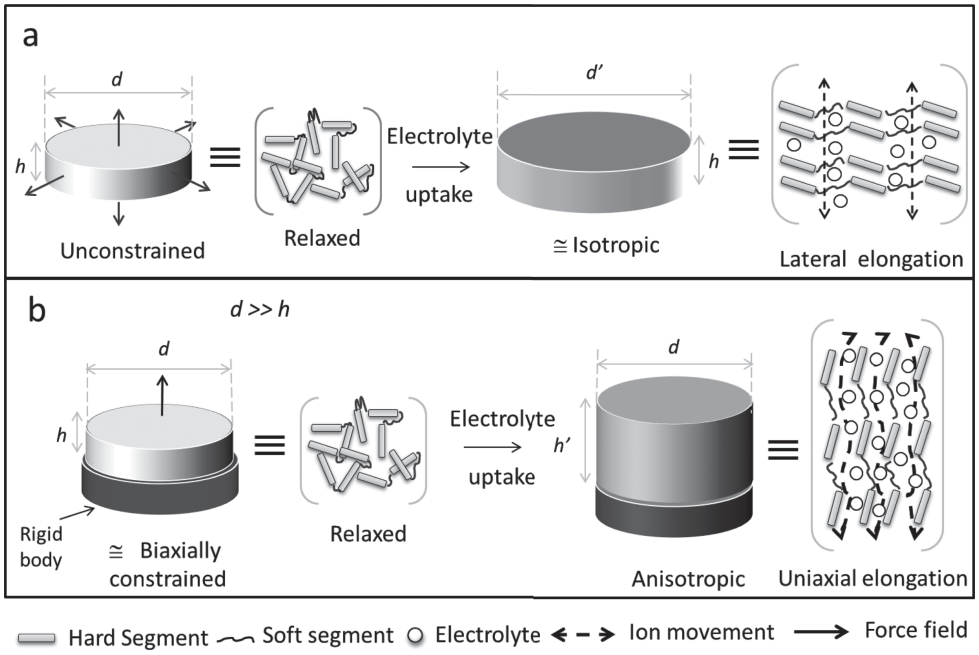

Scheme 1. a) Schematic depicting the volumetric change of a free standing (unconstrained) body undergoing isotropic expansion. This is equated to an elastomer undergoing chain elongation upon liquid electrolyte uptake with a preferential orientation in the transversal plane. b) Volumetric changes of a biaxially constrained body, undergoing anisotropic expansion. This is equated to an elastomeric film undergoing anisotropic elongation upon uptake of electrolyte with a preferential orientation in the direction normal to the constraining plane. In a conventional battery cell configuration, the latter chain orientation could offer an obstacle free inter-chain solvent filled ion transport channels, while in the former orientation, the hard segments restrict ion transport. These orientation proposals are borne out of the Flory-Huggins theory.[22,44]

© 2013 WILEY-VCH Verlag GmbH & Co. KGaA, Weinheim

liquid electrolyte uptake by the host matrix without transversal elongation.

It has been shown that when solid electrolyte in good contact with the electrode's active material, it enables the formation of a stable and compact solid electrolyte interface (SEI) layer and confines its thickness to dimensions where it is not impervious to Li^+ propagation.[23] This layer is crucial in Li-Ion batteries as it prevents excessive electrolyte decomposition by blocking electron transport through itself,[24] inhibits Li dendrites from extending into the anode,[25] and averts graphitic anode exfoliation.[26] Already, vitreous solid inorganic electrolytes have been conformally sputtered onto various electrodes. However, their rigidity, nanoscopic dimensions, and low tensile strength further lower the overall mechanical strength of the final cell.[5,27] Recently, Ajayan and co-workers reported a solution based deposition of a thin poly(methyl methacrylate) (PMMA) separator/electrolyte over one-dimensional nanostructured electrodes, thereby demonstrating such an integration methodology.[28] Their protocol was largely facilitated by the use of an alumina temp.

In this paper, we describe a simple and highly adaptable protocol of integrating a commercially available, mechanically, and thermally robust polyurethane host matrix with graphitic anodes. This high tensile strength (56 MPa)[17b] scratch resistant (shore hardness A = 85) coating, if applied at the electrode manufacturing facility, can further act as an abrasion and moisture barrier to avoid electrode damage and annealing processes required prior to cell assembly. We show that such an assembly allows for a high liquid electrolyte loading without unnecessary transversal volumetric expansions, unlike its non-integrated counterparts. Additional blending of the matrix with non-elastomeric polymers is not required, as the solid active matrix provides additional structural reinforcement and confines excessive swelling into a desired uniaxial perpendicular plane. To the best of our knowledge, we demonstrate for the first time, with convincing experimental evidence, that this elastomer later turned solid electrolyte can be conformally integrated onto both micro and macro-structured electrodes. Unlike conventional gels, once integrated onto the anodic electrode and subsequently infused with liquid electrolyte, our elastomer-based solid electrolyte remains robust, upholds its diameter and displays some element of elasticity. Additionally, the structural integrity of the elastomer is maintained after several charge discharge cycles, while remaining fully integrated onto the electrode, in contrast to a non-integrated electrode that easily disintegrates. Finally, we exemplify that regular Li-ion based electrolytes can be anisotropically infused into elastomer integrated graphitic anodes and, when cycled over several days, the elastomer preserves its integrity and sturdiness. We further propose a roll to roll protocol that can be affected to assemble such cells at large scale as outlined in **Scheme 2**.

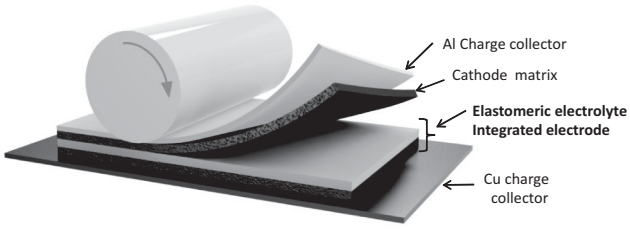

Scheme 2. Roll–roll assembly process of a cell that incorporates an elastomer integrated electrode. Notice that unlike the conventional method for assembling cells with solid electrolyte, the anode is already integrated with the elastomeric anode electrolyte.

2. Results and Discussions

2.1. Thermal Analysis and Electrolyte Uptake

From thermogravimetric analysis (TGA) data, it was determined that the elastomer retained well over 99% of its mass up to 325°C after which a rapid thermal degradation occurred as depicted in **Figure 1**a. This is well above the temperature used to anneal battery electrodes for moisture elimination before cell assembly. The concomitant differential scanning calorimetry (DSC) thermogram exhibited two endothermic peaks at 125 °C and 255 °C, associated with the long range elastomer crystallization and rigid segment micro-crystallizations enthalpies, respectively.[29] The exothermic peaks at 144 °C and 326 °C were consequently ascribed to the respective reverse (melting) effects. Extensive DSC studies of similar polyurethanes after electrolyte uptake have reported T_g values between –60 to –20 °C, signifying that such an elastomer would remain elastic after electrolyte uptake.[19b]

Attempts of carrying out auxiliary contact angle measurement experiments on drops of $LiPF_6$ in a 1:1 mixture of ethylene carbonate and dimethyl carbonate (EC/DMC) on the elastomer film revealed very low angles, ascribed to the excellent wettability of the elastomer by the liquid electrolyte. Electrolyte uptake by both free standing and anode integrated elastomers was monitored quantitatively in weight and dimension, as shown in Figure 1b. Upon submersion, the weight of the free standing elastomer more than doubled within 13 min. Beyond that, only infinitesimal increments occurred, ascribed to the equilibration of the elastomer's tensional and compressional forces. However, when the free standing elastomer was left in excess electrolytic liquid for 8 days, complete dissolution occurred, in contrast to the integrated elastomer which remained rubbery.

Numerous studies on the ionic conductivity of similar systems consistently report values in the range of 10^{-4} to 10^{-2} S cm^{-1} and electrochemical stability up to 4.5 V versus Li/Li^+, which is adequate for Li-Ion battery applications.[26,27c,30] The rapid electrolyte diffusion into the elastomer exemplifies the inherent Li^+ solvability therein, due to its polyether moieties.[23b] Incidentally, its diameter increased in a similar trend, albeit with a lower percentage. In spite of a tremendous volumetric increase, the elastomer remained robust due to its high tensile strength even after drying. In Figure 1c,d, we schematically present the contrasting dimensional changes that occur in the conventional free standing and our anode integrated elastomer.[14] The transversal elongation of the former with respect to electrolyte uptake is illustrated in Figure 1c. By contrast, the seamless integration of our elastomer onto the heterogeneous inelastic active anode imposes an expansion anisotropy on the elastomer such that electrolyte uptake is constrained to the direction normal to the constraining plane,

© 2013 WILEY-VCH Verlag GmbH & Co. KGaA, Weinheim

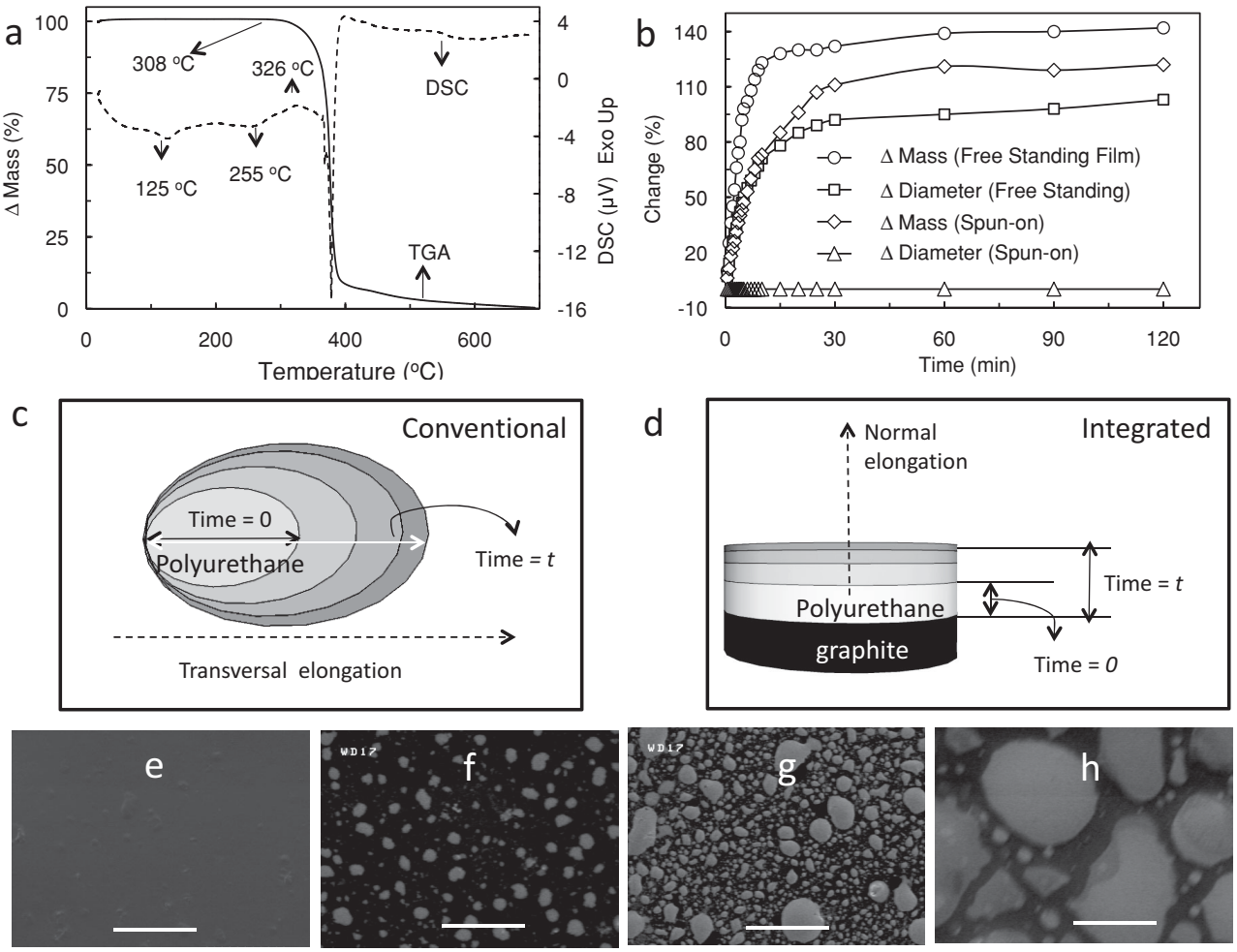

Figure 1. a) Combined TGA and DSC curves of the pure elastomer, exhibiting elastomer stability below 300°C, while the DSC curve exhibits two endothermic transitions at 125 °C and 255 °C and respective exothermic transitions at 144 °C and 326 °C. b) Dimensional and gravimetric changes of the free standing our integrated elastomer as they are infused with 1 M $LiPF_6$ in the EC/DMC electrolytic system. c,d) Illustrations of the dimensional changes of the free standing and integrated elastomer films upon electrolyte uptake. Notice that while the latter experiences a film thickness increase, the former undergoes a predominantly lateral expansion. e) Scanning electron microscopy of the neat elastomer film. Same film after electrolyte uptake for 15 min, g) 30 min, f) 120 min (the scale bars in (c–f) are all 20 μm). The white precipitate is thought to be the electrolytic salt.

as illustrated in Figure 1d. Further, scanning electron microscopy (SEM) images of the elastomer taken after 0, 15, 30, and 120 min, as shown in Figure 1e–h, exhibit the evolution of the elastomer's surface as electrolyte uptake progressed. White precipitates of about 1 μm and 5 μm in diameter, believed to be $LiPF_6$ were noted at the 15 and 30 min, respectively. These precipitates, believed to be partially extended into the elastomer, increased in size with immersion time up to diameters of about 20 μm. This was confirmed by EDS mapping of a similarly prepared sample whereby the molar ratio of fluorine (F) to phosphorous (P) on the grains was found to be ≈5:1, which was close to the theoretical 6:1 ratio of the two elements in pristine $LiPF_6$ salt (Supporting Information). Although these precipitates may have no bearing on the porosity of the elastomer, since the analysis was carried out after film drying, they give an estimate of how much electrolytic salt was infused in the elastomer without rupture. For the elastomer integrated onto the graphitic anode, uptake was slightly sluggish over the same period and only saturated after 30 min, attributed to reduction of the exposed surface area (close to 50% reduction for thin films) as one face of the disk was directly integrated on the graphitic surface. In contrast to the free standing elastomer, the integrated elastomer's diameter did not change. This is particularly important given that, in actual battery applications, it would not have to be trimmed to match the electrode size. Its weight and thickness, however, increased two-fold.

2.2. Dimensional Dynamics of Elastomer/Electrolyte

Further, investigation of the robustness of the heterogeneous graphitic electrode–elastomer interface was investigated by SEM, as shown in **Figure 2**. To conform to the commercially available cell separators, its thickness was maintained between 25–35 μm, as shown in the cross-sectional SEM image of the integrated electrode in Figure 2a. This was achieved by either

© 2013 WILEY-VCH Verlag GmbH & Co. KGaA, Weinheim

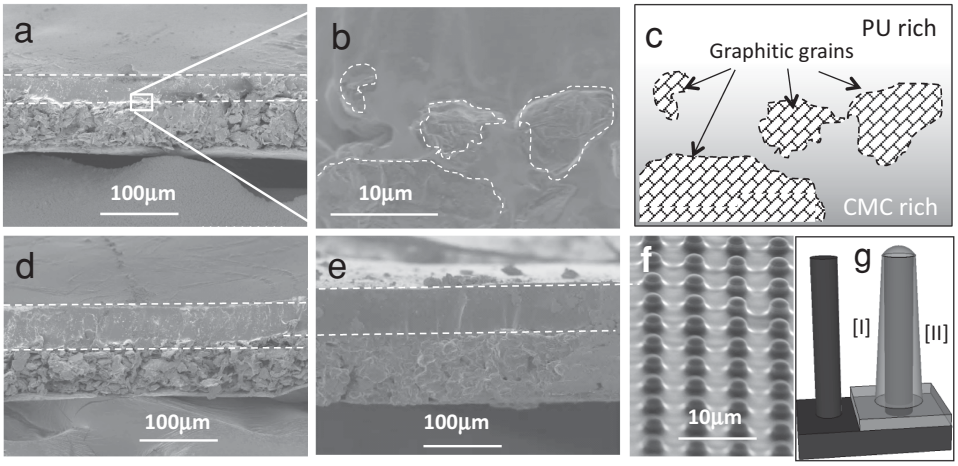

Figure 2. a) Cross-sectional SEM of the electrode depicting the approximate thickness of our spun-on-elastomer. b) A higher magnification of the interface; the graphitic matrix and the elastomer layers are indistinguishable. c) Schematic of (b). The only visible boundaries are those of the graphitic grains, while a gradual transition between anode and elastomer occurs. PU = polyurethane. d) Same electrode as in (a) after $LiPF_6$ in DMC/EC electrolyte uptake. Note that the elastomer thickness almost doubles while that of the graphitic matrix is the same. e) Cross-section SEM image of a similar electrode after extended cycling. Note that the thicknesses of the active matrix and our elastomer have increased as expected but the latter still remains robustly integrated to the former. f) Elastomer conformally integrated onto a microstructured substrate. g) Schematic of the microstructured substrate before [I] and after [II] being conformally coated with the elastomer.

spin-coating or drop-casting of the elastomer solutions over a wide area. Under higher magnification, the elastomer/graphitic anode interface was indistinguishable, an attestation to the good distribution of the elastomer into the graphitic layer as shown in Figure 2b. Only graphitic grain boundaries were distinguishable as outlined by the dotted lines therein, further sketched in Figure 2c. Such a robust integration could only be achieved after a thoughtful material and process design which we developed. We determined that using dimethyl formamide (DMF) as a solvent that mutually dissolves carboxymethyl cellulose (CMC) and the elastomer could greatly facilitate their smooth mixing at the interface. We therefore hypothesize that, upon wetting the electrode, DMF partially dissolved the electrode surface such that, on drop-casting the elastomer solution, a harmonious amalgamation of the two polymers ensued. This was corroborated by an auxiliary experiment in which a solution of equal amounts of the two polymers in DMF (not shown here) did not phase segregate when left standing over several days.

Figure 2d typifies the same interface upon electrolyte uptake. As seen, in spite of almost doubling the elastomer's thickness, it did not delaminate from the graphitic anode. It further remained morphologically even and crack free, an implication of the even electrolytic salt distribution in the host matrix. Figure 2e exemplifies the same elastomer–electrode interface after several months of continuous evaluation in a half cell setting with Li as the counter. The elastomer maintains some of its elasticity even after numerous cycles given that it is still sturdily attached to the electrode. A non-elastic solid electrolyte would not remain crack free upon subjection to the stress and strain associated with expansion and contraction of graphitic anodes during cycling.[31] As seen in Figure 2f, and the ensuing schematic (Figure 2g), even highly structured electrodes and substrates can be conformably integrated with our elastomer without adhesion promoters.

2.3. AC-Impendence and Cyclic Voltammetry Measurements

In-situ AC-impedance measurements of the elastomer during electrolyte uptake were made at 5, 15, 30, 60, 90, and 120 min in order to determine its conductance dynamics. **Figure 3**a depicts the corresponding Nyquist plots. At the 5 minute mark, the Z' value of 13400 ohm was realized, which quickly decreased to 7940 Ω after 15 min. After 45 min, only infinitesimal impedance reductions were observed, attributed to the sluggish electrolyte uptake as corroborated in Figure 1b, due to near attainment of an equilibrium chemical potential between the electrolyte inside and outside the elastomer.[14] After 2 h, the impedance had dropped to 3160 Ω, a mere one order magnitude larger value than that of neat liquid electrolyte (381 Ω). The corresponding computed ionic conductance of the semi-solid electrolyte at 5, 15, 30, 45, 60, 90, and 120 min were 1.49×10^{-3}, 2.52×10^{-3}, 3.6×10^{-3}, 4.28×10^{-3}, 5.25×10^{-3}, 5.28×10^{-3}, and 6.33×10^{-3} S cm^{-1}, respectively, compared to 5.25×10^{-2} S cm^{-1} for the liquid electrolyte, which can be attributed to the high liquid electrolyte loading within the elastomer.[14,32]

Cyclic voltammetry (CV) was then used to evaluate the REDOX properties of our integrated anode versus Li foil for 5 cycles at 1 mV s^{-1} in comparison to a conventional liquid cell.[33] The CV measurements embodied characteristics typical of a graphitic anode. Li^+ ion intercalation into the graphite occurred over a broad potential window starting at 0.4 to 0.0 V while the de-intercalation process commenced at 0.2 to 0.8V.[34] The current responses in the anodic scans from 2 to 5 (not shown here) were slightly higher than that in the first cycle, attributable to the better ionic transport across the graphitic matrix, due to the formation of additional pores after the initial cycle. As expected, similar characteristics were exemplified by the conventional half-cell. The fifth cycles of the two cells were then superimposed as shown in Figure 3b. The two current magnitudes, as

© 2013 WILEY-VCH Verlag GmbH & Co. KGaA, Weinheim

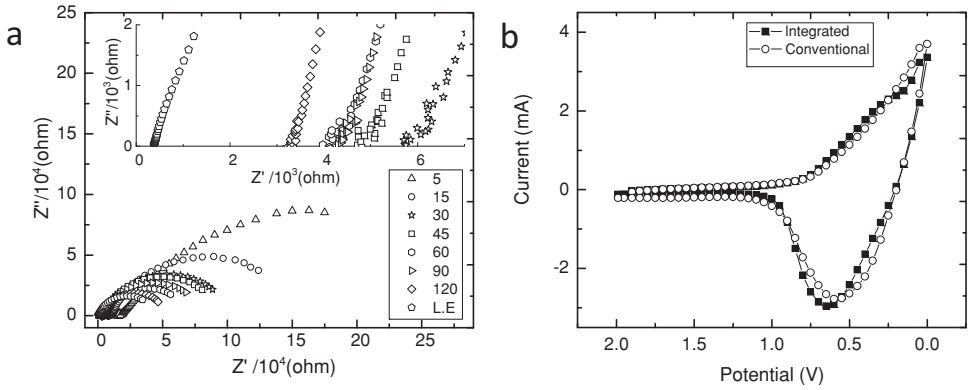

Figure 3. a) Nyquist traces of the elastomer during electrolyte uptake at 5, 15, 30, 45, 60, 90, and 120 min compared to that of neat liquid electrolyte Insert is a close up, b) 5 CVs of half-cell with graphitic anode vs Li foil using 1M $LiPF_6$ in a 1:1M DMC/EC electrolyte at superimposition of the 5th cycles of CVs of half cells made of conventional graphitic anode vs Li foil using 1 M $LiPF_6$ in a 1:1 MDMC/EC electrolyte and that in which an elastomer is first integrated onto graphite, then converted into a semi-solid electrolyte in situ exhibiting similar REDOX processes.

well as the peak potentials, were identical, an indication that ion transport across our solid electrolyte was near identical to that of the liquid electrolyte.

2.4. Areal Charge Discharge Evaluation

Further evaluation the electrochemical performance of the integrated electrode in conjunction with Li-counter in a half-cell configuration was undertaken by subjecting it to several galvanostatic charge–discharge cycles between 0 and 2 V. Initially, a high rate (2 C) was chosen to gauge its initial response to fast charge transport kinetics.[27c,35] Such rates also emulate the conditions required for pulsing and charging most portable devices.[36] **Figure 4**a exemplifies charge–discharge curves of the first 12 cycles of the conventional half-cell. The shapes of the charge–discharge curves are consistent with the work reported by others at the same rate.[37] Its corresponding first charge and discharge areal specific capacities of 0.22 and 0.19 mAh cm^{-2} were realized. These correspond to gravimetric specific capacities of 28.7 and 24 mAh g^{-1} respectively. They quickly dipped by a factor of two in a mere three cycles. In contrast, the initial areal specific charge and discharge capacities of the integrated electrode were 0.32 and 0.16 mAh cm^{-2}, which translated to respective specific gravimetric capacities of 41 and 21 mAh g^{-1}. Although these are only a fraction of the theoretical capacity of graphitic anodes, they are consistent with similar electrodes operated at 2 C.[34] The computed Coulombic efficiencies of 85% and 50% for the conventional and our integrated electrodes, respectively, were realized in their respective first full cycles. The low Coulombic efficiencies for these two half-cells are typical for most graphitic anodes.[38]

The low specific gravimetric charge and discharge capacity of the conventional half-cell over the integrated one could have occurred due to any of the following: i) electrode dewetting, ii) excessive parasitic electrolyte reduction reactions at the anode of the conventional cell that plausibly reduced the magnitude of ions available for intercalation,[39] iii) diminished electrolyte-graphite surface area due to a poor interface and a thicker SEI layer within the conventional half-cell which negatively impact Li-ion diffusivity across it,[23b,40] iv) consumption of Li-ions within the SEI layer of the conventional electrode with its thick SEI layer, leading to a proportionally larger irreversible capacity and capacity fading compared to the integrated electrode,[34] v) negative effects of a strongly solvated Li^+ within the conventional half-cell that more often than not requires a large activation energy for desolvation to occur, which is a rate-determining step in charge transport at the SEI-active matrix (graphite) interface.[41] On the other hand, the possibility of the elastomeric layer storing Li-ions, thus increasing the observed high capacity of our integrated half-cell compared to the conventional cell is not excluded.[42]

The respective charge capacity fade of 55% and 39% for the conventional and our integrated half-cell was compared to a discharge capacity fade of 50% and 42% respectively over the 12 cycles, as exemplified in Figure 4c,d. Figure 4e summarizes the Coloumbic efficiency of the two cells. The conventional cell was in all aspects better (83–90%) compared to 50–85% for our integrated electrode, attributable to the expectedly better ionic conductance of the pristine electrolyte (as opposed to solid state counterpart).

2.5. Specific Charge–Discharge Evaluation

The respective cells' specific charge and discharge capacity changes with respect to cycle number at rates of C/2, C/8, C/12, C/16, and C/20 for 12 cycles are consecutively summarized in **Figure 5**a,b. After cycling at the specified C-rate, the cells were allowed to relax overnight before the next set of experiments. The observed specific gravimetric capacities at the given C-rates are consistent with literature.[34,40a] The specific capacities of the two half-cells at C/2–C/20 were comparable in contrast to 2 C, where our integrated electrode performed significantly better than the conventional one, as shown in Figure 4a,b. We believe that since these C-rates are significantly lower than 2 C, charge diffusion across the thicker SEI layer within the conventional half-cell does not play a significant role because there is

© 2013 WILEY-VCH Verlag GmbH & Co. KGaA, Weinheim

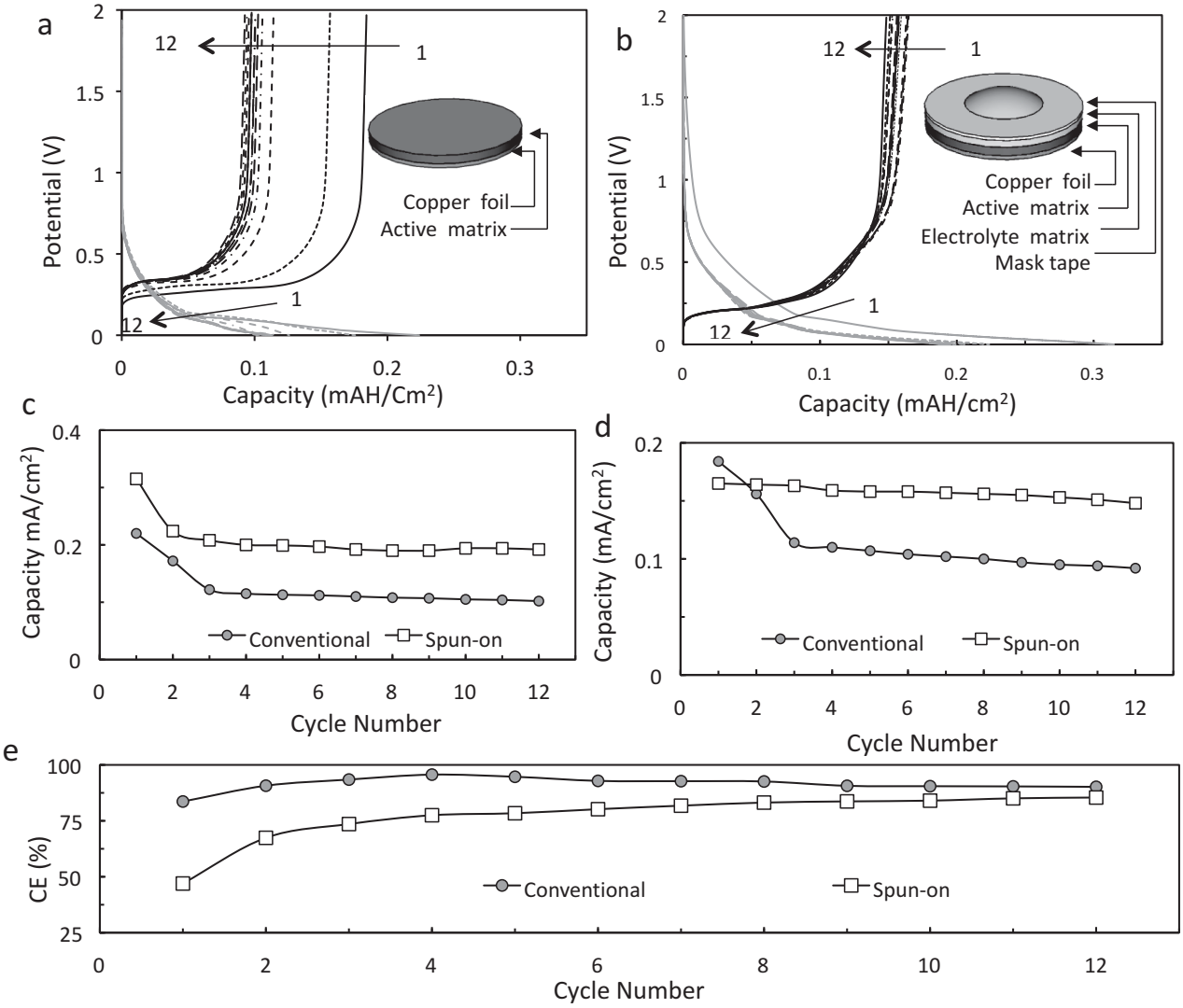

Figure 4. a) Charge–discharge curves of a conventional half-cell with a graphitic anode versus Li foil cathode using 1 M $LiPF_6$ in a 1:1 DMC/EC electrolyte at a C-rate of 2 C. b) Charge–discharge curves of a similar electrode in which the elastomer integrated anode infused with the same electrolyte at the same C-rate. c) Areal specific charge capacity changes vs cycle number for the two half cells, and d) areal specific discharge capacity changes vs cycle number for the two half cells. e) Coulombic efficiencies of the two cells vs cycle number.

enough time for percolation to occur. At C/20, specific charge capacity of the conventional and our integrated electrode, were 360 mAh g^{-1} and 367 mAh g^{-1} respectively, which is close to the theoretical value for graphite.[34] As expected, the Coulombic efficiency of the conventional cell was slightly higher than that of our integrated electrode, especially at high C-rates, which we attributed to poorer ionic conductance of the latter.[43] However, at C/20 their Coulombic efficiencies were almost similar, that is, 97 (our integrated) and 99 (conventional).

2.6. In Situ Selective and Anisotropic Elastomer Activation

We then further investigated selective activation of our integrated graphitic anode as illustrated in the inserted schematic in Figure 4b. SEM images of the masked and exposed sections of our elastomer before and after extended cycling were taken. **Figure 6**a shows the top and cross-sectional images of the integrated electrode before electrolyte infusion demonstrating the thickness and morphological uniformity of the elastomer. Upon disassembly, Figure 6b illustrates the nature of the spun-on elastomer (now partially turned elastomeric electrolyte). On the left side, the electrolyte infused portion that had not been covered with the electrolyte impenetrable tape clearly exhibited a shinier surface. This was consistent with charging of the infused volatiles therein compared to the right side which was darker under the same electron beam. Further, the relatively sharp cross-sectional thickness disparity at the boundary of the activated and inactivated portions corroborates the observation that electrolyte uptake into the elastomer was vertically

© 2013 WILEY-VCH Verlag GmbH & Co. KGaA, Weinheim

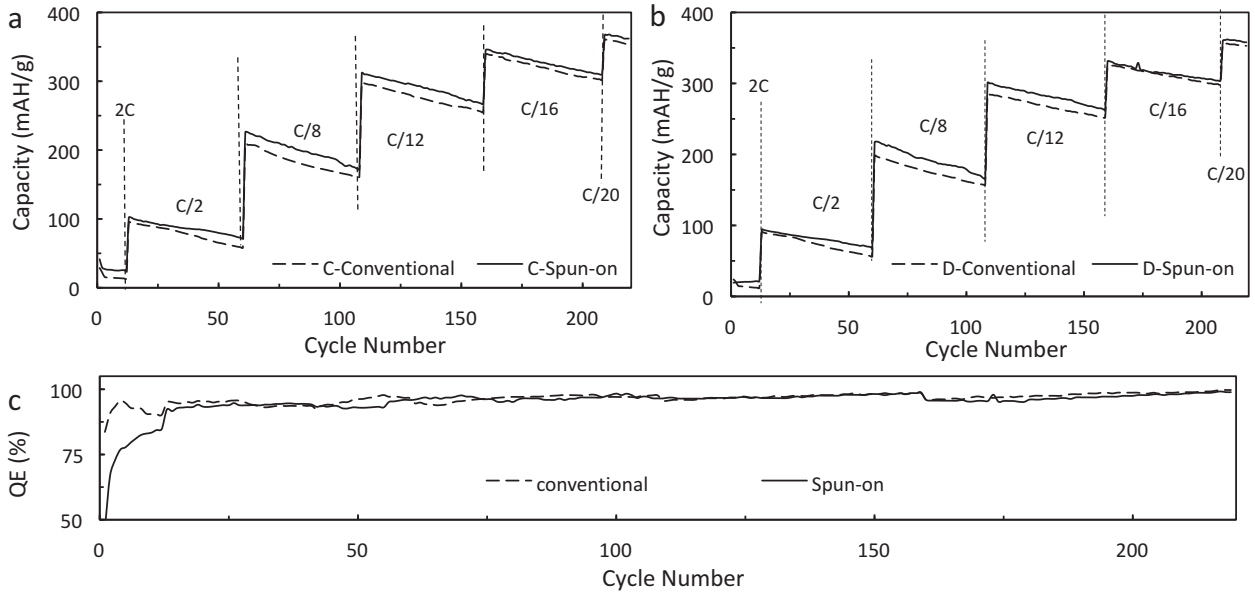

Figure 5. a) Specific gravimetric charge capacity changes vs cycle number of the two half cells. The specified C-rates showing that the integrated electrode has a consistently higher charge capacity compared to the conventional one. b) Specific gravimetric discharge capacity changes vs cycle number of the two half cells. c) Combined consecutive Coulombic efficiencies of the two cells vs cycle number. The conventional half-cell performs slightly higher than the integrated electrode. At each C-rate, the cells were cycled for 12 cycles.

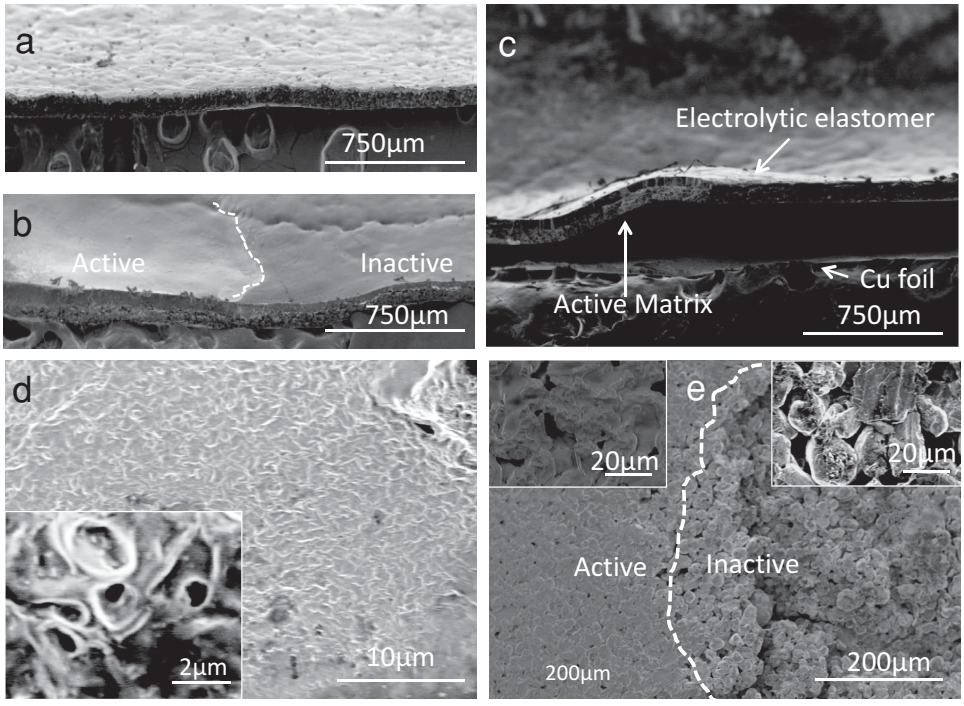

Figure 6. a) SEM image of the elastomer atop the graphitic anode. b) SEM image of an electrode after being selectively activated. Notice the hue and cross-sectional thickness differences in the activated and inactivated portions. c) Integrated electrode after extensive cycling, and the active matrix delaminated from the Cu charge collector is held intact by the elastomer. d) SEM of the elastomer after extended cycling. The insert shows that pores developed. e) SEM of the electrode showing the activated and inactivated sections. The inserts show the nature of the crevices within the active matrix on the active and inactive sections.

© 2013 WILEY-VCH Verlag GmbH & Co. KGaA, Weinheim

confined. This technique of masking and selective electrolyte infusion can be used to prepare micropatterned electrode arrays that can be selectively evaluated, with greater precision and control.

The attractiveness of our integration process is further exemplified in Figure 6c. Here, the active matrix of the conventional electrode evaluated under similar conditions disintegrated upon disassembly (not shown here), possibly due to the stress and strain experienced during the Li-intercalation and de-intercalation processes. By contrast, our integrated electrode remained intact. Even when the electrode partially delaminated from the underlying Cu-foil-current-collector, it did not disintegrate (as shown in Figure 6c). This demonstrates that our unique way of integrating an elastic solid electrolyte into the active matrix, rather than merely sandwiching its free-standing version in between electrodes as is regularly practiced, strengthens the underlying active matrix layer. Further, the interfacial bond between the resultant solid electrolyte and active material is stronger than that between the graphite matrix and Cu foil, as demonstrated by the latter's delamination. We hypothesize that our integration process imparts a substantial level of elasticity onto the active matrix, such that the stress and strain forces the latter experiences during Li^+ insertion and de-insertion processes are well accommodated.[3c]

Upon examining the elastomer after cell evaluation, its morphology remarkably remained outstanding as illustrated in Figure 6d. We only observed the appearance of low density nanopores of about 200 nm in diameter. Their smooth edges and cylindrical nature indicated that their creation was not stress induced, as we would expect for a crystalline material. This further corroborates our finding that the solid electrolyte retains some of its elasticity after extended cell cycling. Topographical SEM images of the interface, exemplifying clean and clear cut distinction between the activated and inactive section of electrode surface, are illustrated in Figure 6e. Further observation of the inserted magnified SEMs elucidated the relatively fewer and smaller crevices on the exposed side of the electrode compared to the unexposed side. These findings suggest that during the integration process, the low viscosity elastomer solution flowed into the inter-particle crevices, thus creating a stronger bond.

3. Conclusions

We have demonstrated a simple yet effective methodology of robustly integrating commercially available elastomer onto a graphitic anode, by exploiting the mutual solvability of the binder within the anode matrix and the elastomer in DMF. We have shown that the solubility of the binder at the surface of the graphite matrix upon exposure to DMF enables it to fuse with the elastomer seamlessly. The scratch resistant elastomer further acts as an abrasion and moisture barrier layer to the electrode. Our elastomer can be conformally applied onto high aspect ratio microstructured substrates without the aid of surface modifiers and adhesion promoters. Our ensuing heterogeneous electrode is flexible and the elastomer can be selectively infused with regular Li-ion based electrolytes in situ, turning it into a solid state elastomeric electrolyte. The gravimetric charge–discharge capacities of this electrode at high rate capabilities are approximately twice that of a conventional electrode. We have shown that even though the Coulombic efficiency of the ensuing electrode is lower at high C-rates, it is comparable to conventional electrodes at low C-rates. Our elastomer retains reasonable elasticity to guarantee mechanical integrity of the entire electrode over prolonged periods of operations while retaining its sturdiness. The good mechanical and elastomeric properties of the elastomer, as well as our integration protocol herein developed, in conjunction with the in-situ conversion technique into an ionically conductive matrix, circumvents pitfalls associated with dimensional increments of the polyurethane elastomers in the transversal plane, upon electrolyte uptake. Our demonstrated method, which is highly adaptable to roll to roll manufacturing, also addresses the fragility of the crystalline gel electrolytes that often crumble upon being subtly perturbed. The challenges in the development of a protocol to circumvent problems associated with poor solid electrolyte–electrode interfaces for both planar and 3D electrodes to facilitate efficient charge transport can be overcome by the protocol outlined herein.

4. Experimental Section

Materials: Lithium foil (3 mm thick) and DMF were obtained from Alfa Aesar and Sigma Aldrich respectively. 1 M lithium hexafluorophosphate in a 1:1 mixture of dimethyl carbonate and ethylene carbonate (1 M $LiPF_6$ in EC/DMC), graphitic anode, and microporous polypropylene cell separator were all obtained from MTI Corporation. The polyurethane elastomer Iro Coat CA-888 was donated by Huntsman Cooperation. Its characteristics include T_g of −37 °C, 100% modulus of 7 MPa, tensile strength of 56 MPa, shore hardness *A* of 85, and is elastic even beyond 600% elongation. Electrode assembly was handled in a MBraun argon filled glove-box. Coin-type half cells (2016R size), were used for rate capability experiments. A CH- Instruments 660-D electrochemical work station was used for electrochemical measurements. Charge–discharge measurements were measured with a MTI 8-channel battery analyzer (BST8-WA).

Thermal Analysis: Thermal properties of the polymer were acquired from TGA and DSC analyses from room temperature to 700 °C at a ramp rate of 20 °C min^{-1}.

Film Preparation: Free standing films of the elastomer with an average thickness on 30 µm were drop cast onto either Si wafers or polyethylene substrates from a 10 wt/vol% solution of the elastomer in DMF at room temperature. They were subsequently dried at 50 °C on a hotplate for 48 h followed by vacuum for 24 h. They were then peeled off the substrates and punched into 1.5 cm diameter disks using a compact precision ring cutter. Alternatively, they were dropcast on commercially available graphitic anodes in a similar way. Beforehand, the graphitic anode was wetted with DMF for 10 min. These were similarly punched into 1.5 cm diameter disks yielding elastomer integrated electrodes.

Liquid Electrolyte Uptake: Elastomeric disks of 1.5 cm diameter with known weights were submerged into commercially available 1 M lithium hexafluorophosphate ($LiPF_6$) in 1:1 mixture of ethylene carbonate and dimethylene carbonate (EC/DC) for a known time in an argon filled glovebox. Percent electrolyte infusion into the elastomer was determined by measuring the gravimetric changes according to Deng et al.[17b] Film diametric changes were calculated according to:

$$\Delta\% = \left(\frac{d_b - d_a}{d_a}\right) \times 100\% \quad (1)$$

where d_a and d_b are the initial and final diameters of the elastomer.

© 2013 WILEY-VCH Verlag GmbH & Co. KGaA, Weinheim

Electrode Integration and Fabrication: A paper punch was used to cut out circular holes with 0.75 cm diameter on the center of a 1.5 cm diameter disk of brother label plastic tape. These were precisely taped onto a 1.5 cm diameter elastomer integrated graphitic anodes prepared as outlined above, such that the central portion of the elastomer coated anode was left open. These were placed onto a split cell with the exposed area facing upwards. About three drops of electrolyte were applied on the exposed elastomer and left over varied durations in a DC saturated chamber. Half-cells were then constructed by incorporating a 1.5 cm diameter lithium disks. A similar procedure was used to prepare cells with no elastomer. However, a 35 µm thick microporous polyethylene cell separator was placed in between the graphite anode and the lithium cathode. Here, two drops of the electrolyte were directly applied on the graphitic anode and left to saturate over varied durations. Alternatively, cells were also prepared without use of the protective tape for comparison purposes.

Cell Evaluations: The in-situ ionic conductivity of the elastomer was measured by electrochemical impedance spectroscopy (EIS) measurements with AC potential amplitude of 5 mV and a frequency range of 1 Hz–100 kHz. The experiment was designed in such a way that, the elastomer could be dipped in and out an electrolytic solution without removal of two stainless steel wires used as electrodes. At high frequency (close to 100 kHz), the corresponding value of the intercept on the real axis (Z' axis) was taken as the intrinsic resistance of the elastomeric electrolyte. Ionic conductivity is calculated according to:

$$\sigma = \frac{L}{RS} \tag{2}$$

where σ is the ionic conductivity, L is the distance between the two electrodes, R is the resistance of the elastomeric electrolyte, and S is the geometric area of the electrode–electrolyte interface.

Cyclic voltammetry was employed to determine the REDOX behavior of the graphitic anodes at a scan rate of 1 mV s^{-1} from 2–0 V over 5 cycles, with graphite being the working electrode and lithium acting as both an auxiliary counter and reference electrode. Chronopotentiometric evaluations were then carried out at difference various C-rates on a 0–2 V potential window. SEM was used to determine the morphological differences in the graphite and the elastomer before, after, and at different treatments.

Supporting Information

Supporting Information is available from the Wiley Online Library or from the author.

Acknowledgements

This work was partially supported by a University of California CITRIS grant, a DARPA AWARE grant, and NSF grant #CMMI-1235592. The authors would like to acknowledge helpful discussion and experimental support of Pallavi Daggumati, Muhammad Ali Qureshi, and Jin Yong Oh of UC Davis, and Dr.Carmen Plapcianu of NIMP, Romania.

Received: April 1, 2013
Revised: May 21, 2013
Published online: June 26, 2013

[1] J. M. Tarascon, M. Armand, *Nature* **2001**, *414*, 359–367.
[2] E. Quartarone, P. Mustarelli, *Chem. Soc. Rev.* **2011**, *40*, 2525–2540.
[3] a) F. T. Wagner, B. Lakshmanan, M. F. Mathias, *J. Phys. Chem. Lett.* **2010**, *1*, 2204–2219; b) A. Patil, V. Patil, D. W. Shin, J. W. Choi, D. S. Paik, S. J. Yoon, *Mater. Res. Bull.* **2008**, *43*, 1913–1942; c) M. Duduta, B. Ho, V. C. Wood, P. Limthongkul, V. E. Brunini, W. C. Carter, Y. M. Chiang, *Adv. Energy Mater.* **2011**, *1*, 511–516.
[4] M. Armand, J. M. Tarascon, *Nature* **2008**, *451*, 652–657.
[5] J. W. Long, B. Dunn, D. R. Rolison, H. S. White, *Chem. Rev.* **2004**, *104*, 4463–4492.
[6] a) N. Yoshimoto, H. Nomura, T. Shirai, M. Ishikawa, M. Morita, *Electrochim. Acta* **2004**, *50*, 275–279; b) C. Gerbaldi, J. R. Nair, G. Meligrana, R. Bongiovanni, S. Bodoardo, N. Penazzi, *Electrochim. Acta* **2010**, *55*, 1460–1467; c) H. S. Kim, S. H. Na, S. W. Eom, S. I. Moon, *Bull. Electrochem.* **2004**, *20*, 439–443.
[7] E. Santaniello, A. Manzocchi, P. Sozzani, *Tetrahedron Lett.* **1979**, *20*, 4581–4582.
[8] a) R. L. Lavall, S. Ferrari, C. Tomasi, M. Marzantowicz, E. Quartarone, A. Magistris, P. Mustarelli, S. Lazzaroni, M. Fagnoni, *J. Power Sources* **2010**, *195*, 5761–5767; b) J. Hassoun, S. Panero, P. Reale, B. Scrosati, *Adv. Mater.* **2009**, *21*, 4807–4810; c) S. Wang, S. Jeung, K. Min, *Polymer* **2010**, *51*, 2864–2871.
[9] a) F. H. Meng, Y. Ding, *Adv. Mater.* **2011**, *23*, 4098–4102; b) D. S. Powers, R. A. Vaia, H. Koerner, J. Serres, P. A. Mirau, *Macromolecules* **2008**, *41*, 4290–4295.
[10] V. R. Basrur, J. C. Guo, C. S. Wang, S. R. Raghavan, *ACS Appl. Mater. Interfaces* **2013**, *5*, 262–267.
[11] J. W. Fergus, *J. Power Sources* **2010**, *195*, 4554–4569.
[12] S. Bandyopadhyay, R. F. Marzke, R. K. Singh, N. Newman, *Solid State Ionics* **2010**, *181*, 1727–1731.
[13] Y.-S. Lee, J. H. Lee, J.-A. Choi, W. Y. Yoon, D.-W. Kim, *Adv. Funct. Mater.* **2013**, *23*, 1019–1027.
[14] M. Osinska, M. Walkowiak, A. Zalewska, T. Jesionowski, *J. Membr. Sci.* **2009**, *326*, 582–588.
[15] M. Quesada-Perez, J. A. Maroto-Centeno, J. Forcada, R. Hidalgo-Alvarez, *Soft Matter* **2011**, *7*, 10536–10547.
[16] a) H. H. Kuo, W. C. Chen, T. C. Wen, A. Gopalan, *J. Power Sources* **2002**, *110*, 27–33; b) T. C. Wen, H. H. Kuo, A. Gopalan, *Macromolecules* **2001**, *34*, 2958–2963.
[17] a) C. Tang, K. Hackenberg, Q. Fu, P. Ajayan, H. Ardebili, *Nano Lett.* **2012**, *12*, 1152–1156; b) N. Wu, Q. Cao, X. Wang, S. Li, X. Li, H. Deng, *J. Power Sources* **2011**, *196*, 9751–9756; c) F. Croce, G. B. Appetecchi, L. Persi, B. Scrosati, *Nature* **1998**, *394*, 456–458.
[18] S. Wang, K. Min, *Polymer* **2010**, *51*, 2621–2628.
[19] a) N. Wu, B. Jing, Q. Cao, X. Wang, H. Kuang, Q. Wang, *J. Appl. Polym. Sci.* **2012**, *125*, 2556–2563; b) R. L. Lavall, S. Ferrari, C. Tomasi, M. Marzantowicz, E. Quartarone, M. Fagnoni, P. Mustarelli, M. L. Saladino, *Electrochim. Acta* **2012**, *60*, 359–365.
[20] T. Takigawa, K. Urayama, Y. Morino, T. Masuda, *Polym. J.* **1993**, *25*, 929–937.
[21] P. A. L. Fernandes, S. Schmidt, M. Zeiser, A. Fery, T. Hellweg, *Soft Matter* **2010**, *6*, 3455–3458.
[22] a) P. J. Flory, J. Rehner, *J. Chem. Phys.* **1943**, *11*, 521–526; b) P. J. Flory, J. Rehner, *J. Chem. Phys.* **1944**, *12*, 412–414.
[23] a) L. Taberna, S. Mitra, P. Poizot, P. Simon, J. M. Tarascon, *Nat. Mater.* **2006**, *5*, 567–573; b) L. J. Fu, H. Liu, C. Li, Y. P. Wu, E. Rahm, R. Holze, H. Q. Wu, *Solid State Sci.* **2006**, *8*, 113–128.
[24] L. Wang, X. Deng, P. X. Dai, Y. G. Guo, D. Wang, L. J. Wan, *Phys. Chem. Chem. Phys.* **2012**, *14*, 7330–7336.
[25] S. Megahed, B. Scrosati, *J. Power Sources* **1994**, *51*, 79–104.
[26] J. O. Besenhard, M. Winter, J. Yang, W. Biberacher, *J. Power Sources* **1995**, *54*, 228–231.
[27] a) D. Ruzmetov, V. Oleshko, P. Haney, H. Lezec, K. Karki, K. Baloch, A. Agrawal, A. Davydov, S. Krylyuk, Y. Liu, J. Huang, M. Tanase, J. Cumings, A. Talin, *Nano Lett.* **2012**, *12*, 505–511; b) D. R. Rolison, J. W. Long, J. C. Lytle, A. E. Fischer, C. P. Rhodes, T. M. McEvoy, M. E. Bourga, A. M. Lubers, *Chem. Soc. Rev.* **2009**, *38*, 226–252; c) A. Aboulaich, R. Bouchet, G. Delaizir, V. Seznec, L. Tortet, M. Morcrette, P. Rozier, J.-M. Tarascon, V. Viallet, M. Dollé, *Adv. Energy Mater.* **2011**, *1*, 179–183; d) H. Zhang, X. Yu, P. Braun, *Nat. Nanotechnol.* **2011**, *6*, 277–281.

© 2013 WILEY-VCH Verlag GmbH & Co. KGaA, Weinheim

[28] S. Gowda, A. Reddy, M. Shaijumon, X. Zhan, L. Ci, P. Ajayan, *Nano Lett.* **2011**, *11*, 101–106.
[29] J. D. Vanheumen, J. R. Stevens, *Macromolecules* **1995**, *28*, 4268–4277.
[30] Y. Xia, W. Zhang, M. Ha, J. H. Cho, M. J. Renn, C. H. Kim, C. D. Frisbie, *Adv. Funct. Mater.* **2010**, *20*, 587–594.
[31] K. Nakamura, M. Yamamoto, K. Okamura, R. M. Mahbubar, Y. Michihiro, I. Nakabayashi, T. Kanashiro, *Solid State Ionics* **2002**, *152*, 241–246.
[32] A. Hayashi, M. Yoshizawa, C. A. Angell, F. Mizuno, T. Minami, M. Tatsumisago, *Electrochem. Solid-State Lett.* **2003**, *6*, E19–E22.
[33] a) I. Geoffroy, A. Chagnes, B. Carre, D. Lemordant, P. Biensan, S. Herreyre, *J. Power Sources* **2002**, *112*, 191–198; b) J. Swiatowska, V. Lair, C. Pereira-Nabais, G. Cote, P. Marcus, A. Chagnes, *Appl. Surf. Sci.* **2011**, *257*, 9110–9119.
[34] R. Yazami, P. Touzain, *J. Power Sources* **1983**, *9*, 365–371.
[35] D. Aurbach, Y. Eineli, *J. Electrochem. Soc.* **1995**, *142*, 1746–1752.
[36] H. Shi, *J. Power Sources* **1998**, *75*, 64–72.
[37] T. D. Tran, J. H. Feikert, X. Song, K. Kinoshita, *J. Electrochem. Soc.* **1995**, *142*, 3297–3302.
[38] J. Cabana, L. Monconduit, D. Larcher, M. R. Palacin, *Adv. Mater.* **2010**, *22*, E170–192.
[39] S. Q. Shi, P. Lu, Z. Y. Liu, Y. Qi, L. G. Hector, H. Li, S. J. Harris, *J. Am. Chem. Soc.* **2012**, *134*, 15476–15487.
[40] a) A. Debart, L. Dupont, P. Poizot, J. B. Leriche, J. M. Tarascon, *J. Electrochem. Soc.* **2001**, *148*, A1266–A1274; b) D. Aurbach, *J. Power Sources* **2000**, *89*, 206–218.
[41] Y. Saito, M. Okano, K. Kubota, T. Sakai, J. Fujioka, T. Kawakami, *J. Phys. Chem. B* **2012**, *116*, 10089–10097.
[42] a) S. Laruelle, S. Grugeon, P. Poizot, M. Dolle, L. Dupont, J. M. Tarascon, *J. Electrochem. Soc.* **2002**, *149*, A627–A634; b) C. L. Liao, Y. H. Lee, S. T. Chang, K. Z. Fung, *J. Power Sources* **2006**, *158*, 1379–1385.
[43] P. Ridgway, H. H. Zheng, A. F. Bello, X. Y. Song, S. D. Xun, J. Chong, V. Battaglia, *J. Electrochem. Soc.* **2012**, *159*, A520–A524.
[44] J. Rehner, P. J. Flory, *Ind. Eng. Chem.* **1946**, *38*, 500–506.

© 2013 WILEY-VCH Verlag GmbH & Co. KGaA, Weinheim